

Theoretical analysis of dynamic chemical imaging with lasers using high-order harmonic generation

Van-Hoang Le,^{1,2} Anh-Thu Le,¹ Rui-Hua Xie,¹ and C. D. Lin¹

¹*J. R. Macdonald Laboratory, Department of Physics, Cardwell Hall, Kansas State University, Manhattan, Kansas 66506, USA*

²*Department of Physics, University of Pedagogy, 280 An Duong Vuong, Ward 5, Ho Chi Minh City, Vietnam*

(Received 10 November 2006; published 20 July 2007)

We report theoretical investigations of the tomographic procedure suggested by Itatani *et al.* [Nature (London) **432**, 867 (2004)] for reconstructing highest occupied molecular orbitals (HOMOs) using high-order harmonic generation (HHG). Due to the limited range of harmonics from the plateau region, we found that even under the most favorable assumptions, it is still very difficult to obtain accurate HOMO wave functions using the tomographic procedure, but the symmetry of the HOMOs and the internuclear separation between the atoms can be accurately extracted, especially when lasers of longer wavelengths are used to generate the HHG. Since the tomographic procedure relies on approximating the continuum wave functions in the recombination process by plane waves, the method can no longer be applied upon the improvement of the theory. For future chemical imaging with lasers, we suggest that one may want to focus on how to extract the positions of atoms in molecules instead, by developing an iterative method such that the theoretically calculated *macroscopic* HHG spectra can best fit the experimental HHG data.

DOI: [10.1103/PhysRevA.76.013414](https://doi.org/10.1103/PhysRevA.76.013414)

PACS number(s): 33.80.Rv, 42.65.Ky

I. INTRODUCTION

In the microscopic world, chemical reactions and biological transformations occur on the time scale of the order of picoseconds or less. Understanding the intermediate steps of these reactions or transformations has been the dream of physical and chemical scientists [1,2]. While x-ray and electron diffraction have served well to image the structure of large molecules, current technology limits such tools for time resolution to tens of picoseconds to subpicoseconds [3,4], making them less suitable for time-dependent studies. On the other hand, infrared lasers of durations of tens to subfemtoseconds are becoming widely available today; thus, it is natural to ask whether femtosecond lasers can be used for dynamic chemical imaging of molecules. Since the wavelength of infrared lasers is much larger than the interatomic spacings, these lasers cannot be used for diffraction measurements directly. Nevertheless, recent experiments [5] have shown that the shape of the highest occupied molecular orbitals (HOMOs) can be revealed by measuring the alignment dependence of the ionization rates by subfemtosecond lasers. Similarly, limited experimental evidence and theoretical calculations so far have also shown that high-order harmonic generation (HHG) can reveal the structure of molecules [6–8], including even two-center interference [9–11]. Self-diffraction from the rescattering electron following laser ionization has also been suggested for imaging molecules [12–14]. Despite many such discussions in the literature in the past decade, few real demonstrations have been achieved so far.

In a recent paper, Itatani *et al.* [15] reported that they have reconstructed the highest occupied molecular orbital of N₂ molecules accurately using the tomographic procedure from the measured HHG spectra. Using a weak laser beam first to partially align N₂ molecules, a more intense short probe pulse (30 fs) was then used to generate high-order harmonics. The polarization direction of the probe pulse was varied

from a parallel to a perpendicular direction with respect to the pump pulse. The retrieved HOMO wave function has been shown to be in surprisingly good agreement with the HOMO calculated from a quantum chemistry code. In a more recent paper, taking that HHG is generated from a many-electron N₂ molecule, it was further shown [16] that the reconstructed wave function records the image of the Dyson orbital plus exchange contributions from the inner shells.

The success of Itatani *et al.* has generated a lot of interest. If it is generally applicable, it would offer a means for time-resolved dynamic chemical imaging at the resolution of tens to subfemtoseconds. However, a number of works have expressed skepticism recently [17–19]. Rigorously speaking, in quantum mechanics, the ground-state wave function is not measurable alone since any measurement would invoke final states. The tomographic procedure used by Itatani *et al.* relies on the approximation that the continuum states of the molecule in the recombination process be represented by plane waves, an approximation that is well known to be invalid in photochemistry, unless the continuum electron's energy is in the keV range. This is not the case for HHG in the plateau region where the photons are from a few tens to about 100 eV.

The starting point of Itatani *et al.* is the three-step model of high-order harmonic generation [20–22]. The harmonic yield is assumed to be given by the product of three terms: one is the initial tunneling ionization rate, the next is the propagation of the free electron in the laser field, and the third is the recombination of the electron with the ion to emit high-order harmonics. By assuming that the first two steps are nearly independent of whether the target is molecular or atomic as long as they have nearly identical ionization potentials, Itatani *et al.* were able to extract the recombination dipole matrix element for individual N₂ molecules from the measured HHG in the plateau region, as well as their variation with angles. These dipole matrix elements are then used

to obtain the molecular wave function using the tomographic imaging method.

Two important approximations are used in this tomographic procedure. First, the dipole moment of individual molecules in the direction parallel and perpendicular to the laser's polarization can be obtained from the measured macroscopic HHG. For this, they assumed that the harmonics in the direction parallel to the laser polarization satisfies the complete phase matching condition. Experimentally this is done by placing the gas jet after focusing the laser, thus eliminating the contribution to HHG from long trajectories [23,24]. They did not measure HHG in a direction perpendicular to the laser's polarization, but a dipole moment in the perpendicular direction was assumed. In practice, if the molecules are fully aligned—i.e., all pointing in the same direction in space—then the measurement of macroscopic HHG in the perpendicular direction would allow the determination of the dipole moment in the perpendicular direction. For molecules that are only partially aligned, such as those aligned by a pump laser, it is not straightforward to extract the perpendicular dipole moment of each molecule from the measured macroscopic HHG.

The second important approximation by Itatani *et al.* is that the continuum wave functions in the recombination dipole matrix elements can be approximated by plane waves. This approximation is at the heart of the tomographic procedure. Implicit to this also is that the dipole moment is available over the complete spectral range of the harmonics. This is not so since the useful harmonics are usually limited to the plateau region only.

In this paper we examined the assumptions used in the tomographic procedure. We used the model of Lewenstein *et al.* (Lewenstein model) [22] to calculate the HHG for fixed molecules with different alignment angles with respect to the laser polarization. In this model, the dipole matrix element is calculated using plane waves for the continuum states. We thus take the calculated HHG from the Lewenstein model to be the “experimental” data and follow the procedure of Itatani *et al.* to extract the “experimental” dipole matrix elements. If both models are exact, the “experimental” dipole matrix element thus obtained should be identical to the “exact” theoretical ones which are calculated using plane waves for the continuum states and the HOMO for the initial state. In reality, we found that the “experimental” dipole matrix element agrees with the theoretical one only in a limited spectral range—in the plateau region. With such a limited range, we found the HOMO wave functions derived from the tomographic procedure to be approximate. Even though the accuracy can be improved by using HHG generated with lasers of longer wavelength to extend the plateau region, we were unable to obtain accurate HOMO wave functions.

In view of the failure in obtaining accurate HOMO wave functions, we next turn to the possibility of using HHG to extract some information on the structure of a molecule. We note that in chemical imaging it is not essential to reconstruct the wave function of a molecule. A great deal is understood if the positions of the atoms in the molecule can be determined at intermediate time steps. We thus ask what partial information of a molecule can be revealed by the tomographic procedure under the most favorable conditions assumed

in our model. Using lasers with wavelength of 1200 nm to generate plateau harmonics from N₂ and O₂ molecules at different internuclear distances, we showed that the internuclear distances obtained from the retrieved HOMO wave function is good to better than a few percent. Furthermore, the geometry and the symmetry of the HOMO, including the nodal surfaces, can also be retrieved. Such precision is more than adequate for dynamic chemical imaging and warrants further test for complex molecules where the positions of some atoms undergo a large change, in processes such as isomerization or dissociation, and where the time scale of transformation is of the order of tens of femtoseconds.

The rest of this paper is arranged as follows. In Sec. II we describe the theoretical methods and assumptions used for the present tomographic imaging of molecules using high-order harmonic generation of aligned molecules by lasers. Section III presents the results of extracting HOMO wave functions and the internuclear separations. In Sec. IV we reexamine the assumptions and address the intrinsic limitations of the tomographic imaging method. We showed that these limitations are not easily removed in real applications, making it difficult to apply the tomographic method for chemical imaging in general. In Sec. V, we suggest alternative methods for imaging molecules with HHG, based on the iterative procedure. Assuming that the HHG for a single polyatomic molecule can be calculated accurately, the propagation effect and the effect of partial alignment of the molecules can be taken into account by standard methods. Thus macroscopic HHG can be calculated for each configuration of atoms in the molecule which can then be compared to the experimentally measured HHG. Since HHG can be generated for different alignment angles of the molecules using lasers of different wavelengths, an optimum atomic configuration can be derived by the set that best fits the experimental HHG. We note that in typical chemical reactions, only a few atoms change positions significantly. Thus the number of parameters that have to be determined is small. We then give examples of the isomerization of acetylene C₂H₂ and of hydrogen cyanide HCN to show the alignment dependence of the HHG of these molecules under isomerization. In the last section we summarize our conclusion on the tomographic procedure and discuss future plans for studying dynamic chemical imaging with lasers. Atomic units $m=e=\hbar=1$ are used throughout the paper, unless otherwise indicated.

II. THEORETICAL METHODS

A. Generation of HHG using the Lewenstein model

In this paper, in order to generate the HHG spectra from molecules with fixed alignments, we use the Lewenstein model, as extended by Zhou *et al.* [6]. Without loss of generality, we assume that the molecules are aligned along the x axis in a laser field $E(t)$, linearly polarized on the x - y plane with an angle θ with respect to the molecular axis. The parallel component of the induced dipole moment can be written in the form

$$D_{\parallel}(t) = i \int_0^{\infty} d\tau \left(\frac{\pi}{\epsilon + i\tau/2} \right)^{3/2} [\cos \theta d_x^*(t) + \sin \theta d_y^*(t)] \\ \times [\cos \theta d_x(t - \tau) + \sin \theta d_y(t - \tau)] E(t - \tau) \\ \times \exp[-iS_{st}(t, \tau)] a^*(t) a(t - \tau) + \text{c.c.}, \quad (1)$$

where $\mathbf{d}(t) \equiv \mathbf{d}[\mathbf{p}_{st}(t, \tau) - \mathbf{A}(t)]$ and $\mathbf{d}(t - \tau) \equiv \mathbf{d}[\mathbf{p}_{st}(t, \tau) - \mathbf{A}(t - \tau)]$ are the transition dipole moments between the ground state and the continuum state, and $\mathbf{p}_{st}(t, \tau) = \int_{t-\tau}^t \mathbf{A}(t') dt' / \tau$ is the canonical momentum at the stationary points, with \mathbf{A} the vector potential. The perpendicular component $D_{\perp}(t)$ is given by a similar formula with $[\cos \theta d_x^*(t) + \sin \theta d_y^*(t)]$ replaced by $[\sin \theta d_x^*(t) - \cos \theta d_y^*(t)]$ in Eq. (1).

The quasiclassical action at the stationary points for the electron propagating in the laser field is

$$S_{st}(t, \tau) = \int_{t-\tau}^t \left(\frac{[\mathbf{p}_{st}(t, \tau) - \mathbf{A}(t')]^2}{2} + I_p \right) dt', \quad (2)$$

where I_p is the ionization potential of the molecule. In Eq. (1), $a(t)$ is introduced to account for the ground-state depletion.

The ground-state electronic wave functions were obtained from the GAMESS code [25]. Within the single-active-electron (SAE) approximation, we take the HOMO for the ‘‘ground state;’’ the transition dipole $\mathbf{d}(\mathbf{k})$ is given as $\langle \mathbf{k} | \mathbf{r} | \Psi_0 \rangle$. The continuum state is approximated here by a plane wave $|\mathbf{k}\rangle$. This model has been shown to be able to interpret the experimental results so far for N_2 , O_2 [6,26], and CO_2 [10,27,28]. In this paper we neglect the effects of depletion; i.e., we assume $a(t - \tau) = a^*(t) = 1$. A laser peak intensity of $2 \times 10^{14} \text{ W/cm}^2$ and duration of 30 fs [full width at half maximum (FWHM)] are used throughout this paper.

B. Procedure of tomographic imaging

In the tomographic procedure, suggested by Itatani *et al.* [15], the intensity of the emitted HHG is approximated by

$$S(\omega, \theta) = N^2(\theta) \omega^4 |a[k(\omega)] \mathbf{d}(\omega, \theta)|^2. \quad (3)$$

Here $\mathbf{d}(\omega, \theta) = (2\pi)^{-3/2} \int d\mathbf{r} \Psi_0(\mathbf{r}; \theta) \mathbf{r} \exp[ik(\omega)x]$ is the transition dipole between the HOMO and the continuum state, approximated by a plane wave with $k(\omega) = (2\omega)^{1/2}$; $a[k(\omega)]$ is the amplitude of the continuum plane wave of returned electrons; and $N(\theta)$ is the number of ions produced. $\Psi_0(\mathbf{r}; \theta)$ represents the HOMO, rotated by angle θ (the Euler angle between molecular axis and the laser polarization direction). Note that in Eq. (3) perfect phase matching was assumed in the experimentally measured spectra. This equation can be understood as a further approximation to the three-step model [29]. In the case of strong-field tunneling ionization, it can be assumed that the continuum electron wave packet depends weakly on the molecular structure, but rather on the ionization potential only. Thus, one can get rid of $a[k(\omega)]$ by measuring the HHG from the reference atoms with the same I_p (for N_2 the reference atom is Ar; for O_2 it is Xe).

From the measured HHG and ionization data one can extract the transition dipole $\mathbf{d}(k, \theta)$ by using formula

$$|\mathbf{d}(k, \theta)| = N(\theta)^{-1} |\mathbf{d}_{ref}(k)| \sqrt{S(\omega, \theta) / S_{ref}(\omega)}, \quad (4)$$

with $\mathbf{d}_{ref}(k)$ being the transition dipole moment of the reference atom. From Eq. (4) we can extract only the amplitude of the dipole moment. However, it is well known [30] that the minimum of the harmonic signal and a π phase jump

occur at the same harmonic order. Following Itatani *et al.*, we assume that the dipole changes sign when its absolute value goes through a minimum close to 0.

In this study we will start with HHG from *individual* molecules which were calculated using the Lewenstein model. This allows us to bypass the issues related to phase matching and other macroscopic effects for the time being. Following Itatani *et al.* we obtain the $\mathbf{d}(\omega, \theta)$ from Eq. (3) except replacing $N^2(\theta)$ in the equation by $N(\theta)$ (since phase matching is not used for a single molecule). The ionization rates $N(\theta)$ are calculated using the molecular tunneling theory (MO-ADK) [33].

One major difference from Itatani *et al.* is that in our calculations we use the dispersion relation

$$k = \sqrt{2(\omega - I_p)}, \quad (5)$$

with I_p being the ionization potential. The question about including or not including I_p in Eq. (5) was discussed in a number of papers (see, for example, [31,32]); it is a question of how to relate the energy of the recolliding electron with the energy of the emitted photon. For radiative recombination or photoionization, Eq. (5) is the correct relation, with k being the momentum of the electron in the asymptotic region. In the Lewenstein model the recolliding electron does not see any potential from the ion, so $k^2/2$ is also the kinetic energy of the electron near the nucleus. Indeed we found that the deduced dipole moment from HHG calculated using the Lewenstein model works well only when Eq. (5) was used. In Itatani *et al.*, the relation $k = \sqrt{2\omega}$ was used, but their dipole moment was extracted from the experiment.

From the dipole moment parallel and perpendicular to the polarization direction, we first rotate the two components to the molecular frame. The wave function is then obtained by using the Fourier slice theorem [34]. The basic formulas for the tomographic procedure,

$$x\Psi(x, y) = \int_0^\pi d\theta \int_0^{+\infty} d\omega e^{ik(x \cos \theta + y \sin \theta)} \times [\cos \theta d_x(\omega, \theta) + \sin \theta d_y(\omega, \theta)], \quad (6)$$

$$y\Psi(x, y) = \int_0^\pi d\theta \int_0^{+\infty} d\omega e^{ik(x \cos \theta + y \sin \theta)} \times [-\sin \theta d_x(\omega, \theta) + \cos \theta d_y(\omega, \theta)], \quad (7)$$

can then be used to obtain the HOMO in the molecular frame. Note that here and in the following for the wave function integrated along the third direction we use the notation

$$\Psi(x, y) \equiv \int_{-\infty}^{+\infty} \Psi_0(x, y, z) dz. \quad (8)$$

In principle, the two equations (6) and (7) are equivalent. In practice, however, incomplete dipole moment data would give different results from Eqs. (6) and (7). We take the results to be the mean from the two equations. If we do not know the symmetry of the molecule, the HHG should be measured over the whole alignment range, from 0° to 180° . For homonuclear diatomic molecules the symmetry allows

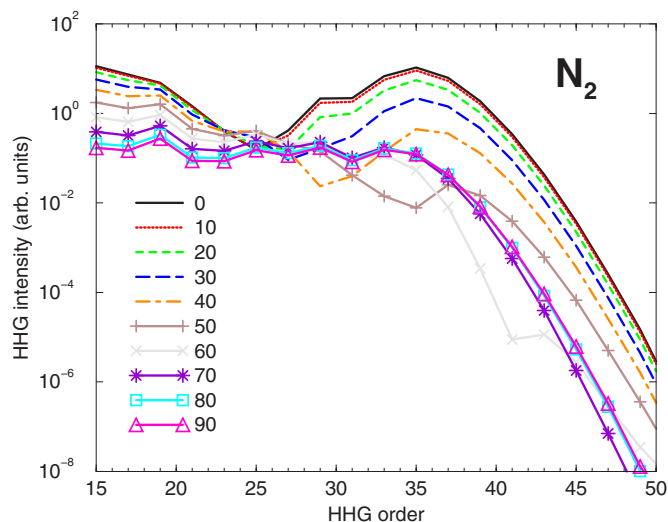


FIG. 1. (Color online) HHG spectra with parallel polarization (with respect to the laser polarization direction) from N_2 aligned at ten different angles between 0° and 90° . A laser wavelength of 800 nm and intensity of 2×10^{14} W/cm 2 are used.

us to consider data from 0° to 90° only. Furthermore, from the investigation of tomographic transformations (6) and (7) using “exact” theoretical dipole moments we found that an angular step of $\Delta\theta=5^\circ$ is good enough for extracting the wave function accurately. Thus, instead of integration over the whole range, we use the summation over the 19 angles from 0° to 90° only.

III. RESULTS AND DISCUSSION

A. Alignment dependence of HHG for N_2 and O_2

In this paper, we generated HHG spectra using the Lewenstein model, extended for molecules, as described in Sec.

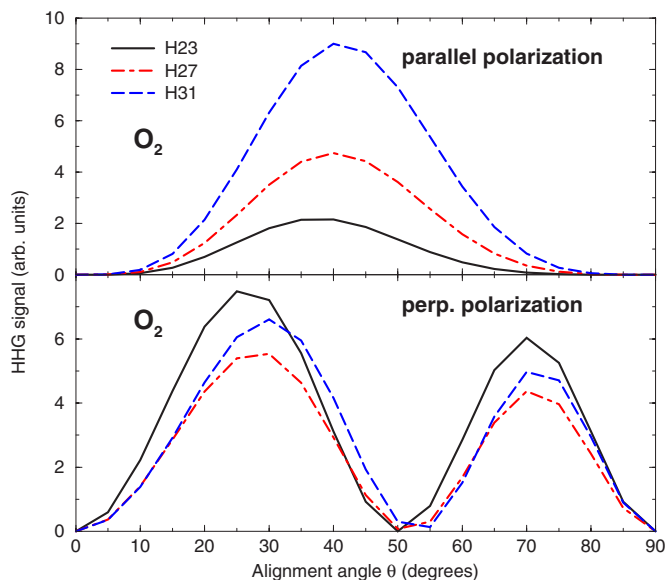


FIG. 3. (Color online) Same as in Fig. 2, but for O_2 .

II A. In Fig. 1, we show the HHG intensities along the direction parallel to the laser polarization for N_2 . Here the molecules are assumed to be fixed in space and the directions of laser polarization are varied from 0 to 90° (in step of 10°) with respect to the molecular axis. The laser wavelength is 800 nm. Note that our results are for single molecules and only odd harmonics are used. For each $(2n+1)$ th harmonic, we integrated the calculated harmonic spectrum from the $(2n)$ th to $(2n+2)$ th harmonics. For the tomographic imaging we need the harmonic yields in the direction perpendicular to the laser polarization as well. Figures 2 and 3 show the alignment dependence of some selective harmonic orders for N_2 and O_2 . Both polarizations are presented. For parallel polarization, the HHG signals are peaked near parallel alignments

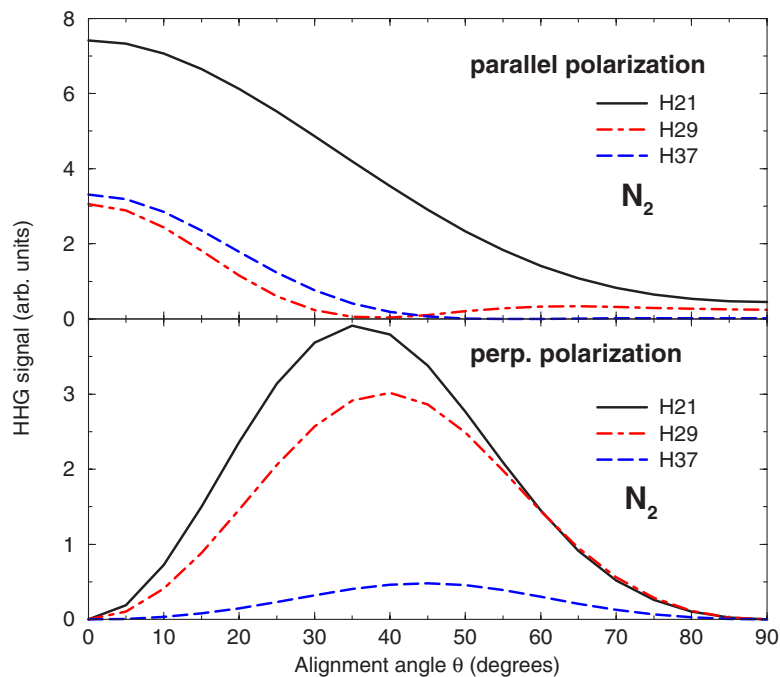


FIG. 2. (Color online) Alignment dependence of selective HHG orders for parallel (top) and perpendicular (bottom) polarizations from N_2 . The laser parameters are the same as for Fig. 1.

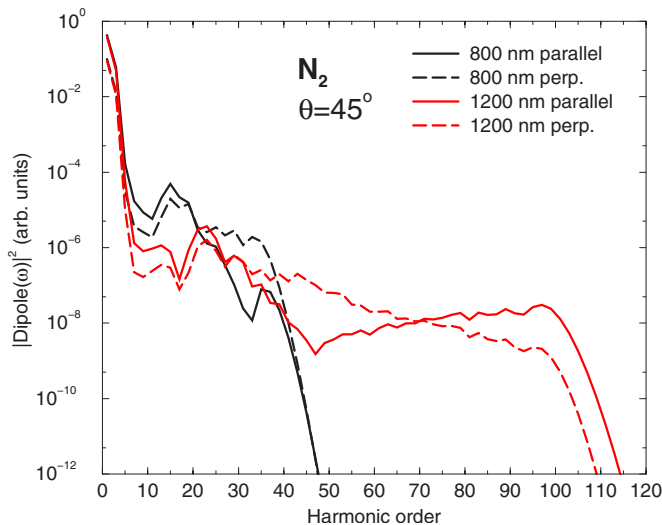


FIG. 4. (Color online) HHG spectra from N_2 aligned at 45° for 800-nm and 1200-nm lasers. Laser intensities of $2 \times 10^{14} \text{ W/cm}^2$ are used in both cases.

for N_2 and about 45° for O_2 . For perpendicular polarization, the HHG signals of N_2 are largest near 45° .

To compare the HHG calculated here directly with those measured by Itatani *et al.* [15] is difficult. Their data are from the macroscopic medium such that the propagation effect is included. Furthermore, the molecules from the pump beam are only partially aligned. Nevertheless, by assuming phase matching and that the molecules are fully aligned, they extracted the dipole moment of the individual molecules from the macroscopic HHG. In Itatani *et al.* the HHG in the perpendicular direction was not measured, but a maximal HHG intensity near 45° was used implicitly [35]. This assumption is consistent with our calculated results for N_2 shown in Fig. 2. For O_2 , our calculations show that the perpendicular HHG intensities almost vanish near 45° and peak at two intermediate angles near 30° and 70° .

In reconstructing the HOMOs, we typically use 19 alignment angles from 0 to 90° (in step of 5°). This is also the typical setup used in the experiments by Itatani *et al.* [15]. We found that using a finer angular grid does not improve the results.

As we will show, in order to improve the quality of the reconstructed HOMOs, one would like to use the HHG over an extended plateau region. It is better not to use higher laser intensities, since it would result in depletion of molecules to distort the simple model [Eq. (3)]. Instead, we choose to use a laser of longer wavelength—say, of 1200 nm. We chose the same peak intensity of $2 \times 10^{14} \text{ W/cm}^2$ as the 800-nm laser. In Fig. 4, we present HHG spectra from N_2 aligned at 45° for 800 nm (black curves) and 1200 nm (red curves). Clearly, the plateaus are extended to much higher harmonics. We note, however, that one harmonic order is 1.55 eV for the 800-nm laser and 1.03 eV for the 1200-nm laser.

B. Extracted dipole matrix elements

First, we use the HHG spectra obtained in Sec. III A (to be called “experimental” in the following) for N_2 in the case

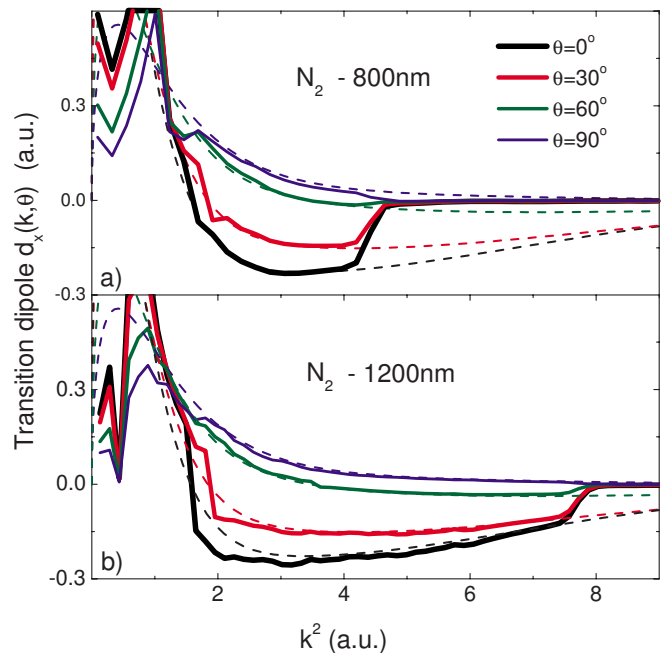


FIG. 5. (Color online) x component of the transition dipoles of N_2 obtained from HHG data (solid lines) in comparison with the theoretical ones (dashed lines) in the case of the 800-nm laser (a) and 1200-nm laser (b).

of an 800-nm laser to extract the dipole moment in the laboratory frame by using Eq. (4). $\text{Ar}(3p)$ (with $I_p = 15.76 \text{ eV}$) is used as the reference atom, as suggested by Itatani *et al.* [15]. The data are available for 19 angles θ in the range of $[0-90^\circ]$. These extracted “experimental” dipole moments will be compared to those calculated theoretically. For demonstration, in Fig. 5(a) we show the “experimental” and theoretical results of $d_x(k, \theta)$ for the angles θ of 0° , 30° , 60° , and 90° . Similar results are shown in Fig. 6(a) for the y component of the dipole $d_y(k, \theta)$. In order to compare with the theoretical data, we have normalized the x component of the dipole at $k^2 = 2.5$ for $\theta = 0$. The normalization factor is then fixed and used for all the other alignment angles as well as for y components. This normalization factor is also used for N_2 with the 1200-nm laser.

From Figs. 5(a) and 6(a) we see that the “experimental” dipoles compare well with the theoretical ones in the range of $k^2 = [0.9-4.2]$, which is equivalent to the useful range of HHG from H17 to H47 for the 800-nm laser. The lower limit H17 is due to the inaccuracies in the Lewenstein model for low harmonics, while the upper limit H47 is due to the harmonic cutoff. For the 800-nm laser and intensity of $2 \times 10^{14} \text{ W/cm}^2$ the cutoff position is at about H35 for N_2 , as can also be seen in Fig. 1.

We can enlarge the useful region of HHG by using longer-wavelength lasers. In Figs. 5(b) and 6(b) we show the “experimental” dipole moments in the case of a 1200-nm laser with the same intensity. The useful dipole moments now cover the range $k^2 = [1.0-7.5]$, or H27–H113, of the 1200-nm laser. We note that the agreement between the “experimental” and theoretical dipoles appears to be better for higher plateaus. This is not entirely surprising since one should ex-

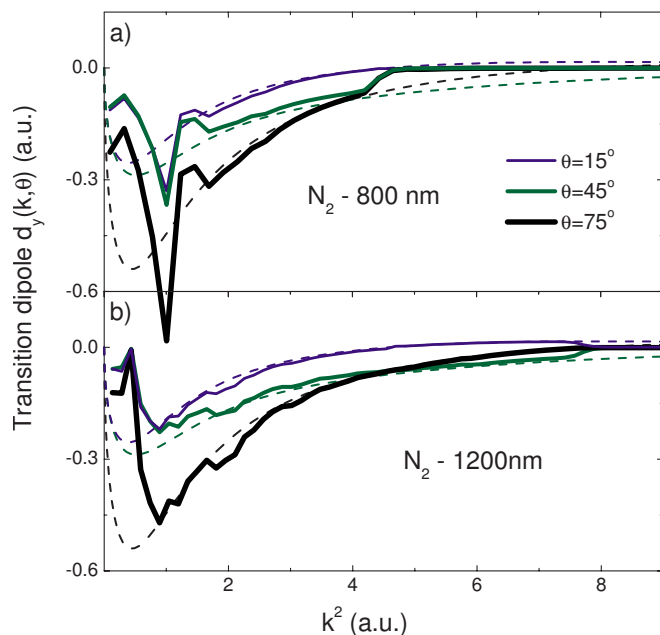


FIG. 6. (Color online) Same as in Fig. 5 but for the y component.

pect the simple model, Eq. (3), to agree better with the Levenstein model near the cutoff, where the contribution from single returns dominates [29].

In Fig. 7 we show the extracted dipole moments for O_2 molecules using the 1200-nm laser. In this case $Xe(5p)$ (with $I_p=12.13$ eV) is chosen as the reference atom. The normalization is done in a similar fashion as for N_2 , but here we

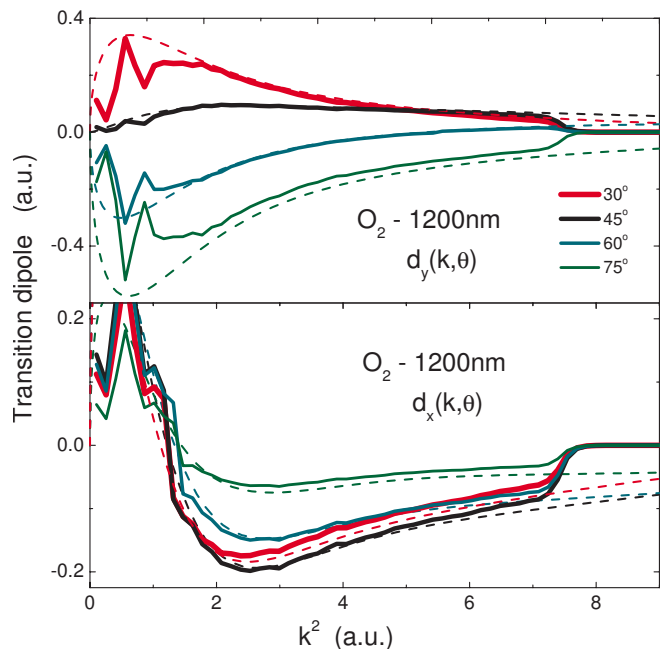


FIG. 7. (Color online) The transition dipole matrix element of O_2 extracted from HHG data (solid lines) in comparison with the theoretical ones (dashed lines) in the case of the 1200-nm laser. The upper and lower panels are for y and x components, respectively.

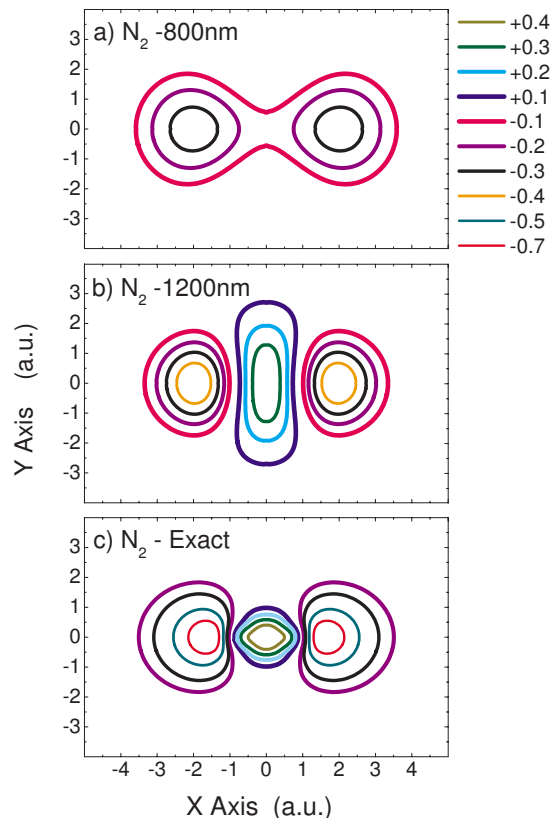


FIG. 8. (Color online) The contour plot of the wave function of N_2 obtained from HHG data in the useful range H17–H47 of the 800-nm laser (a), from HHG data in the useful range H27–H113 of the 1200-nm laser (b), and from the theoretical transition dipole in the range $k^2=[0-100]$ (c).

chose to normalize the y component of the dipole at $k^2=2.0$ for $\theta=45^\circ$. We see that the results are also comparable with the theoretical data in the range of $k^2=[1.0-7.5]$ corresponding to the useful range of HHG from H25 to H109. The difference in the cutoff positions is due to the different ionization potentials of N_2 (15.58 eV) and O_2 (12.03 eV).

It should be noted that for O_2 the extracted dipole moments for the angles near 0° and 90° do not agree well with the theoretical data. It is related to the accuracy of the small ionization rates and small HHG yields in the small angles and near 90° . Note that the plane-wave approximation (PWA) is also questionable near these angles, where the HOMO of O_2 has nodal surfaces. However, it will be shown in the next section that these inaccuracies do not affect much the wave function obtained by the tomographic procedure.

C. Retrieving wave functions by the tomographic procedure

We next examine the retrieved wave function from the extracted “experimental” dipole moment. We emphasize that in the following the wave function is understood as integrated over the z direction (in the molecular frame) as given in Eq. (8). In Fig. 8(a) the contour plot for the wave function of N_2 obtained from the HHG by the 800-nm laser is shown.

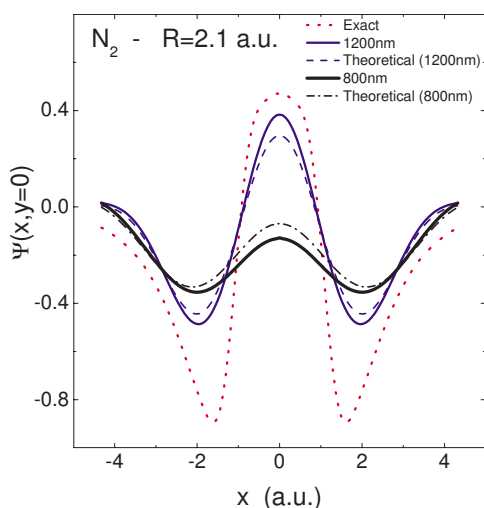


FIG. 9. (Color online) N_2 wave function $\Psi(x, y=0)$. The solid (dashed) curves correspond to the extracted (theoretical) wave function, respectively. The theoretical wave functions are obtained using the tomographic procedure with the same range as for the extracted wave functions. The range is $k^2=[1.0-7.5]$ for the 1200-nm laser (upper solid and dashed curves) and $k^2=[0.9-4.2]$ for the 800-nm laser (lower solid and dashed-dotted curves). For comparison we also plot the converged wave function obtained with the range $k^2=[0-100]$ (dotted curve).

The harmonics used are from H17 to H47. In Fig. 8(b), the wave function extracted from the HHG by the 1200-nm laser is shown, using harmonics orders from H27 to H113. The converged wave function obtained from the tomographic procedure using the theoretical dipole moments in the large range of $k^2=[0-100]$ is shown in Fig. 8(c). This is exactly the ground-state molecular wave function used in the calculation of the HHG. In the following we will call the HOMOs that are obtained from the GAMESS and used to generate HHG spectra “exact” wave functions.

By comparing the three figures in Fig. 8, we see that the result from the 800-nm laser is not good enough, such that even the nodal surfaces are not reproduced. This is due to the limited range of momentum space covered by the H17–H47 harmonics used in the tomographic imaging. For the 1200-nm case, the retrieved wave function resembles the “exact” one quite well, in terms of the orbital shape and the nodal surfaces. This clearly illustrates that the tomographic procedure will work better if longer-wavelength lasers are used, such that the plateau region can be extended over many harmonics. For a more quantitative comparison, we compare the wave functions along the internuclear axis derived by using the various approximations. In Fig. 9, the “exact” results are compared to the wave functions obtained from the 800-nm and 1200-nm lasers. For each wavelength, we compare the wave functions derived by using the dipole moments obtained from the “experimental” HHG data and from the theoretical calculations, but within the same range of k^2 . Clearly the derived wave functions using the same range of k^2 are very close to each other. This indicates that the dipole moment extracted using the simple three-step model, Eq. (3), works well at least within the Lewenstein model. To avoid

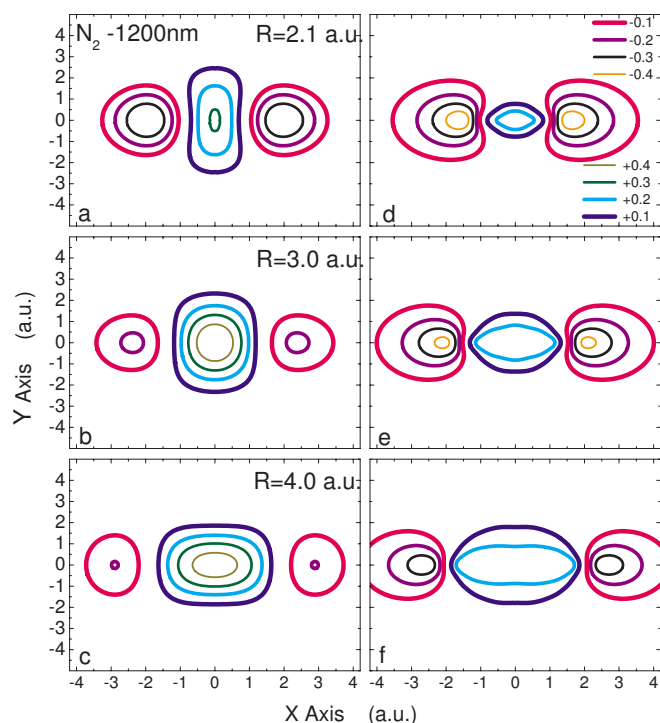


FIG. 10. (Color online) Contour plot of the wave functions of N_2 with the internuclear distance $R=2.1, 3.0,$ and 4.0 , extracted from HHG data (left panels), as compared with the exact ones (right panels).

confusion, we emphasize here that the results shown in Fig. 9 are obtained using Eqs. (6) and (7) and plotted without any artificial vertical shift.

The results in Figs. 8 and 9 indicate that the tomographic imaging method works reasonably well when a 1200-nm laser is used to generate the HHG. We test the procedure for two additional internuclear separations $R=3$ a.u. and $R=4$ a.u. In Fig. 10 we compare the wave functions retrieved from the HHG, using the same range of HHG from H27 to H113. Comparing to the “exact” wave functions, we see that the positions of the nodal surfaces, and the symmetry of the wave functions, are all quite nicely reproduced. Note that in this and the following figure for contour plot of the wave functions, for convenience, we have renormalized the wave functions to 1. It appears that the tomographic procedure fails to correctly reproduce the electron density distributions. This is especially true for $R=3$ and 4 a.u., where it overestimates the distribution between the two nuclei. We note, however, that this is largely due to the limited range of harmonics available. The calculations using the theoretical dipoles with the same range of k (or harmonics) indeed show a similar trend.

We further test the tomographic procedure for the O_2 molecule whose HOMO has different symmetry (π_g instead of σ_g in N_2 case). We used a 1200-nm laser to generate the HHG spectra. The results for the equilibrium distance $R=2.3$ and two other internuclear separations $R=3$ and 4 a.u. are shown in Fig. 11. In this case we notice that the π_g orbitals are well reproduced, and the internuclear separations, as estimated by the distances between the peaks along

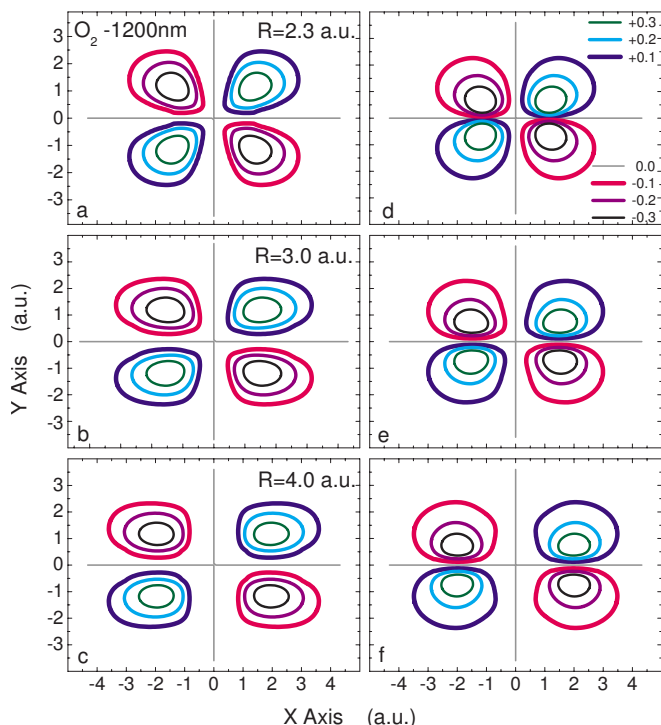


FIG. 11. (Color online) Same as for Fig. 10 but for O_2 with $R = 2.3$ (top panels), $R = 3.0$ (middle panels), and $R = 4.0$ (bottom panels).

x axis, appeared to be quite accurate as well. In fact, we have tested the procedures for $R = 3.5, 4.5,$ and 5.0 a.u. as well. The deduced internuclear distances from the HHGs are shown in Fig. 12. In Table I, the details of the numerical results are shown. The input R and the internuclear distance R^* read from the two peaks of the retrieved wave functions are compared. When a large range of k^2 (0–25 a.u.) in the theoretical dipoles is used in the tomographic procedure, the internuclear separations can be extracted to better than 1%. Using the smaller range of k^2 of 1.0–7.5 a.u., corresponding to H25–H109, we obtained R^* accurate to a few percent, except for the $R = 2.3$ case, which is still good to about 10%.

The relatively good agreement between the retrieved and “exact” wave functions is not entirely surprising. This is because Eq. (3) can be considered as an approximation to the

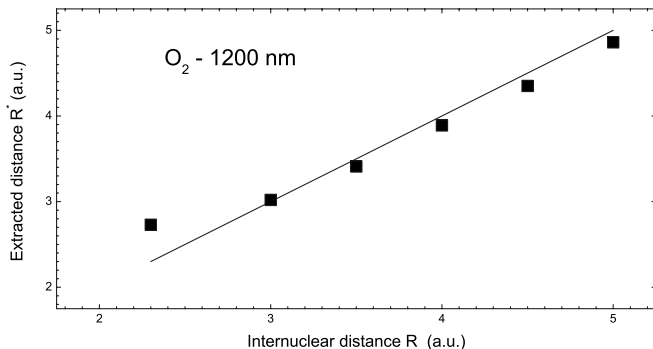


FIG. 12. Internuclear distance of O_2 extracted from HHG data using the 1200-nm laser.

TABLE I. Internuclear distance of O_2 extracted from HHG data using 1200 nm laser. R —internuclear distance as input; R^* —extracted distance using the tomographic procedure. The top row corresponds to the case when “experimental” dipoles are used, the two bottom rows correspond to when the theoretical dipoles are used.

Input R	2.3	3.0	3.5	4.0	4.5	5.0
Extracted R^* , $k^2 = [1-7.5]$	2.73	3.02	3.41	3.89	4.35	4.86
Theor. R^* , $k^2 = [1-7.5]$	2.37	2.92	3.34	3.89	4.35	4.92
Theor. R^* , $k^2 = [0-25]$	2.31	3.01	3.48	3.98	4.48	4.97

Lewenstein model used to generate our “experimental” data. In particular, this agreement cannot be used to justify the PWA, since this approximation is used in both models. On the other hand, one should keep in mind that the Lewenstein model has been shown to be able to interpret the main features of the measured HHG spectra for atoms and simple molecules [6,28,29]. We will discuss in details the limitations of this approach in the next section.

IV. INTRINSIC AND PRACTICAL LIMITATIONS OF THE TOMOGRAPHIC PROCEDURE

In this section we reexamine the assumptions made in the tomographic procedure, following Itatani *et al.* [15]. The starting point of the method is the Fourier slice theorem, Eqs. (6) and (7), which gives a mathematical identity between $\Psi(x, y)$ and the dipole matrix elements $d(k)$ in the direction parallel and perpendicular to the laser’s polarization, with the condition that the transition dipole $d(k)$ be given by $\langle k|r|\Psi_0(r)\rangle$ —i.e., the final continuum states be represented by plane waves. Operationally, the dipole matrix elements are to be obtained from experiments, for example, using high-order harmonics generated from aligned molecules, with the laser’s polarization direction varying from parallel to perpendicular, with respect to the alignment direction of the molecules, as carried out by Itatani *et al.*

We now examine the assumptions and limitations encountered in the practical implementation of the tomographic imaging method.

(i) *Limitation of the available experimental spectral range.* The Fourier slice theorem requires that the dipole matrix elements be measured for the whole spectral range, while the usable range from the HHG is limited to the small plateau region. In Figs. 8–11 we show the effect on the retrieved wave functions if a truncated spectral range is used. For the small plateau region available from HHG generated by 800-nm lasers, we conclude that accurate wave functions cannot be obtained, but significant improvement can be made if the HHG generated by 1200 nm or longer wavelengths are used. We comment that in general by introducing a filter function, the accuracy of the retrieved HOMO can be improved [16,34].

(ii) *Limitation of the approximate three-step model [Eq. (3)] for extracting molecular transition dipoles from the measured HHG spectra.* The link between the HHG yields and the “experimental” dipole moments of an individual

molecule which are used in retrieving the molecular wave function of the initial state is given by Eq. (3)—an equation based on the three-step model of the high-order harmonic generation. Equation (3) was not derived from a rigorous HHG theory, so its validity can only be checked empirically. In Eq. (3), the propagation effect was included by assuming perfect phase matching, an approximation which will be addressed later. Given that Eq. (3) is correct, how to interpret the derived “experimental” dipole matrix element $|d(\omega, \theta)|$? In Itatani *et al.*, they interpreted it as the dipole matrix element to be used in the Fourier slice theorem, Eqs. (6) and (7). This amounts to approximating the “exact” continuum states of a molecule by plane waves over the whole spectral range, a very poor approximation well known from photochemistry.

In this paper, taking advantage of the success of the Lewenstein model in obtaining the main features of the measured HHG spectra for atoms and simple molecules [6,28,29], we used the Lewenstein model to generate the “experimental” spectra. We showed that in that case Eq. (3) is reasonably valid; see the comparisons in Figs. 5–7. Clearly, within our approach, we cannot check the validity of the PWA since it is used in both models. We note, however, that even if one can get the transition dipole without the PWA, one would need to drastically modify the tomographic procedure—namely, to modify or even abandon Eqs. (6) and (7), which are valid only for the PWA.

A further limit of Eq. (3) is that it gives only the absolute values of the dipole matrix element. For simple linear molecules, the dipole matrix elements are real such that one can just change the sign whenever the absolute value goes through a near-zero minimum, as adopted by Itatani *et al.* For more complex molecules, the dipole moments can become complex and it would be difficult to extract the phase information. As for measurement of the relative phase of high harmonics, important progress has been achieved recently [36–38].

Finally, the multielectron effect should be included in the model. Progress in this direction has also been achieved [16,19].

(iii) *Limitations from the macroscopic effects.* The high-order harmonics measured in the laboratory are from the coherent emission of light from many molecules. Equation (3) was written down under the perfect phase matching condition, but how well is it met in actual experimental conditions, especially from partially aligned molecules? We note that in applying Eqs. (6) and (7), both parallel and perpendicular components of the HHG are needed. This can be done in principle if the molecules are fully aligned—i.e., all are pointing in a fixed direction in space. Such a condition cannot be reached by the pump laser pulse where molecules are only partially aligned. Thus the angles between the laser’s polarization and the molecules in the ensemble are not all the same, making it very difficult to extract the perpendicular component of the dipole moment of the individual molecule from the measured HHG signal. Note that for an unaligned ensemble of molecules, the perpendicular component of HHG vanishes. In Itatani *et al.*, the molecules were assumed to be fully aligned in the direction of the pump pulse. They did not measure the perpendicular component of HHG, but

the perpendicular component of the dipole moment was assumed. It turns out that the form they assumed is very close to what we calculated using the Lewenstein model, shown in Fig. 2(b). Note that in our present model study we did not face the macroscopic issues since we derived “experimental” dipole matrix elements from HHG due to a single molecule fixed in space only.

V. CHEMICAL IMAGING WITH HIGH-ORDER HARMONIC GENERATION

A. Alternative methods of chemical imaging

In Sec. III C, with our most optimistic assumptions, we have shown that the HOMO wave function cannot be accurately retrieved based on the tomographic method since the spectral range provided by the plateau harmonics is too limited. On the other hand, the symmetry of the HOMO and the internuclear distances between the two atoms are accurately reproduced from the retrieved wave function, especially when lasers with longer wavelengths—say, 1200 nm—are used. Such information is comparable to what one can obtain from electron or x-ray diffraction experiments. On the other hand, since HHG can be generated with femtosecond lasers of duration of the order of 10 fs or less, the retrieval of even such limited information can be very useful in probing the time dependence of a chemical transformation at a time resolution of the order of tens to subfemtoseconds. Thus further investigations of possible dynamic chemical imaging with HHG by femtosecond lasers are warranted.

In the future, however, we believe that dynamic chemical imaging will be developed along a different route. As discussed in Sec. IV, the steps involved in obtaining single-molecule dipole moments from macroscopic HHG rely on many assumptions which are difficult to remove. At present, we suggest that dynamic chemical imaging with HHG proceed as follows. We assume that the initial configuration of the molecule in the ground state is known from the conventional imaging method. Experimentally the alignment-dependent HHG from the ground state of such a molecule will first be measured, and theoretical calculations will be performed to make sure that the experimental data at this initial configuration are well described. Under chemical transformation, our goal is to locate the positions of the atoms as they change in time, by measuring their HHG spectra at different time delays, following the initiation of the reaction. Assuming that such HHG data are available experimentally, the task of dynamic chemical imaging is to find ways to extract the intermediate positions of all atoms during the transformation and, in particular, to identify the important transition states of the reaction. This will be done by the iterative method.

In the iterative method, we will first make a guess as to the new positions of all atoms in the molecule. A good guess is to follow the reaction coordinates along the path where the potential surfaces have the local minimum. Existing quantum chemistry codes (see, for example, Refs. [25,39]) provide good guidance as a starting point. For each initial guess the HHG from single molecules will be calculated. Then the propagation effect and the alignment of molecules are taken

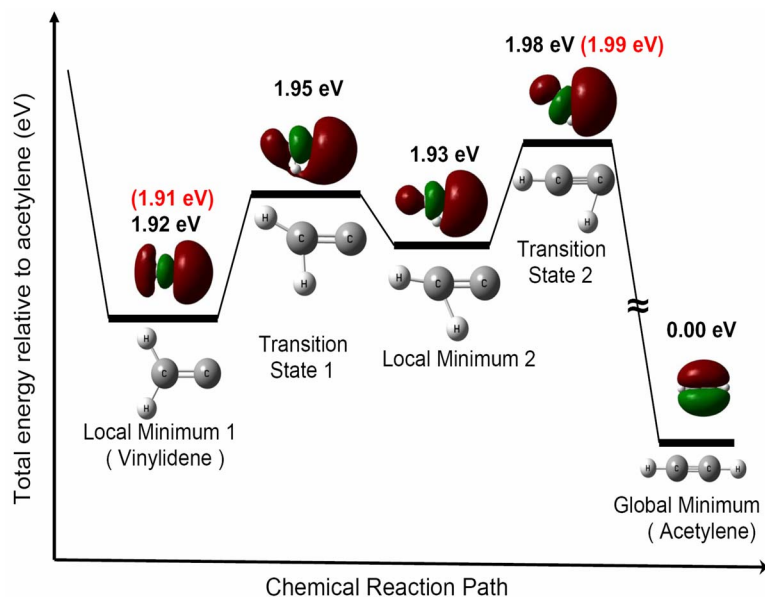


FIG. 13. (Color online) Reaction path of acetylene to vinylidene calculated by DFT with hybrid PBE1PBE functional and AUG-cc-pVTZ basis set. The values in parenthesis are from experiment [42].

into account. The resulting macroscopic HHG is then compared to the experimental data to find atomic configurations that best fit the experimental data. Recall that for each time delay the harmonics can be measured for many different angles between the aligning laser and the probe laser. Different wavelengths of the lasers can also be used. At present, we believe that HHG should be measured along the probe laser's polarization direction only, since the perpendicular component tends to be severely averaged out when molecules are only partially aligned. In principle, the phase of each harmonic can also be measured experimentally [38]. For the chemical imaging purpose, however, we think it is easier to use different wavelengths to generate a larger data set for retrieving the atomic configurations instead.

For the methods suggested above to work, a relatively accurate and efficient theoretical model for calculating HHG from single molecules is needed. Direct solution of the time-dependent Schrödinger equation for molecules in a laser field, even within the single-active-electron model is out of the question. On the other hand, a model such as the Lewenstein model is very efficient. Therefore, at the first stage, one might still use the Lewenstein model or its modifications to generate the theoretical data. It is straightforward to include the propagation effect and the anisotropic distributions of molecules. Thus, if the macroscopic HHG's can be calculated efficiently with reasonable accuracy, the large set of experimental HHG data can then be analyzed to retrieve the atomic configurations at each time step efficiently. We emphasize that in this iterative procedure, the number of parameters that are to be determined is small since only the positions of the atoms that undergo large changes are to be determined.

We summarize that with this method, there are a number of advantages over the tomographic method: (i) There is no need to assume that the continuum states be (incorrectly) represented by plane waves. (ii) There is no obvious need to measure HHG along both the parallel and perpendicular directions. (iii) The method is based on a fitting procedure, not

a Fourier transformation, such that a limited spectral range like the plateau harmonics may be adequate. For the tomographic method the whole spectral range is needed. (iv) The propagation and alignment effect of the molecules can straightforwardly be incorporated in the fitting process.

B. Outlook of chemical imaging with HHG

The method we have suggested above for chemical imaging formally requires an accurate and efficient theoretical method for calculating the HHG of a complex molecule. In a chemical reaction involving "complex" molecules, normally only a few atoms make a large change in positions. Such changes often modify the HOMOs significantly since the symmetry of the molecule is altered, resulting in a significant change in the alignment dependence of the HHG. We note that such changes are typically accounted for by the Lewenstein model already. Thus even before a more accurate theory of HHG becomes available, the procedure outlined in the previous subsection can be tested at least qualitatively.

As an example, consider the isomerization of acetylene to vinylidene [41–43]. Figure 13 shows the simplified possible reaction path of the isomerization that we calculated by using density functional theory [44] with the hybrid exchange-correlation functional of Perdew, Burke, and Ernzerhof (PBE1PBE) [45] and Dunning's correlation consistent basis set augmented correlation consistent polarization valence triple zeta (AUG-cc-pVTZ) [39]. It is in excellent agreement with Ref. [43]. This path involves the well-known transition state TS2 [42]. To reach TS2 from acetylene, at least about 2 eV is needed. Before reaching the vinylidene there is one additional local minimum (LM2) and one additional transition state (TS1) in the potential surface. The positions of the atoms and the shape of the HOMO for each of these special configurations are shown in the figure. Note that the binding energy and the HOMO for acetylene are very different from the other four. Such differences can be easily revealed from the "alignment" dependence of HHG. In Fig. 14 we show the

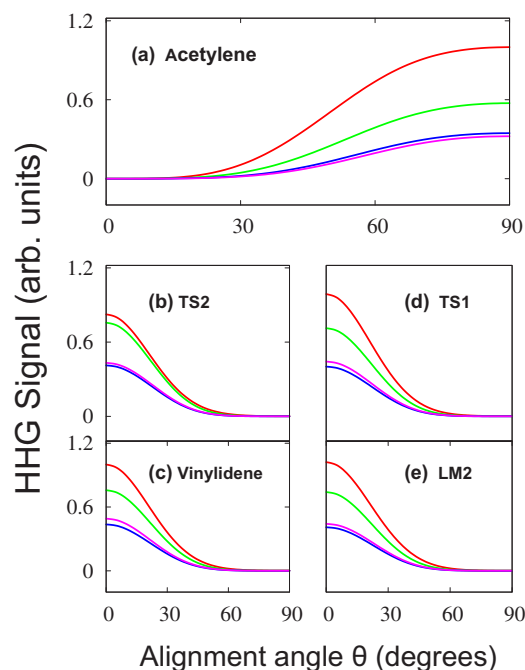


FIG. 14. (Color online) Predicted angular dependence of the 21st, 25th, 29th, and 31st harmonic yields in the plateau region for C_2H_2 isomers: (a) acetylene (from top to bottom), (b) TS2, (c) vinylidene, (d) TS1, and (e) LM2. For (b)–(e), from top to bottom, the curves represent the 21st, 25th, 31st, and 29th harmonic.

HHG calculated for these different isomers. The alignment angle is defined to be between the C-C axis and the laser polarization direction. Except for the linear acetylene, the HHG for the other planar molecules should depend on the ϕ angle which is between the plane of the molecule and the plane of the C-C axis and the laser's polarization. In Fig. 14, this ϕ dependence has been integrated over.

The results in Fig. 14 illustrate the potential and the limitations of using the HHG for imaging molecules. While it is

relatively easy to identify acetylene from vinylidene by the alignment dependence of the HHG yields, it is difficult to distinguish vinylidene from other transient molecules TS1, TS2, and LM2. Although the atomic arrangements for TS2, LM2, and TS1 are quite different from vinylidene, the major features of the HOMO from each of these “molecules” are relatively similar. Since HHG, at least within the simplest model, is generated from the HOMO only, it is to be understood as a probe of the highest occupied molecular orbital, rather than a probe of the positions of the atoms in the molecule, as from the diffraction method. Thus, in a way, imaging by HHG is more similar to ($e, 2e$) momentum spectroscopy [46,47]. While it may be possible to use HHG to distinguish vinylidene from TS2, LM2, and TS1, by carefully analyzing the dependence of HHG on the alignment angle θ and the azimuthal angle ϕ , or by using lasers with different wavelengths, the procedure is likely much more demanding. On the other hand, in a typical reaction, a vibrational wave packet is created. Since the potential surfaces of these four states are quite close to each other, unique identification of the atomic configurations of these four isomers as stationary states may be an oversimplification. Nevertheless, other imaging methods would be needed to map out the full evolution from acetylene to vinylidene. The transformation away from the acetylene, on the other hand, would be very easy to identify using the HHG.

Before closing, we offer one more example—the isomerization of hydrogen cyanide HCN to hydrogen isocyanide HNC [48]. Figure 15 gives the local potential minima, the shape of the HOMO, the atomic configurations, and the contour plot of the potential energy surface calculated by using density functional theory (DFT) [44] with Becke's three-parameter Lee-Yang-Parr hybrid functional (B3LYP) [49] and 6-311+G(2df,2pd) Gaussian-type basis set [39]. The latter provides information on the reaction path from the linear HCN to the linear HNC, via a transition state of a coplanar molecule as sketched. A fair large energy of 2.1 eV is needed to reach the transition state. Note that the HOMOs

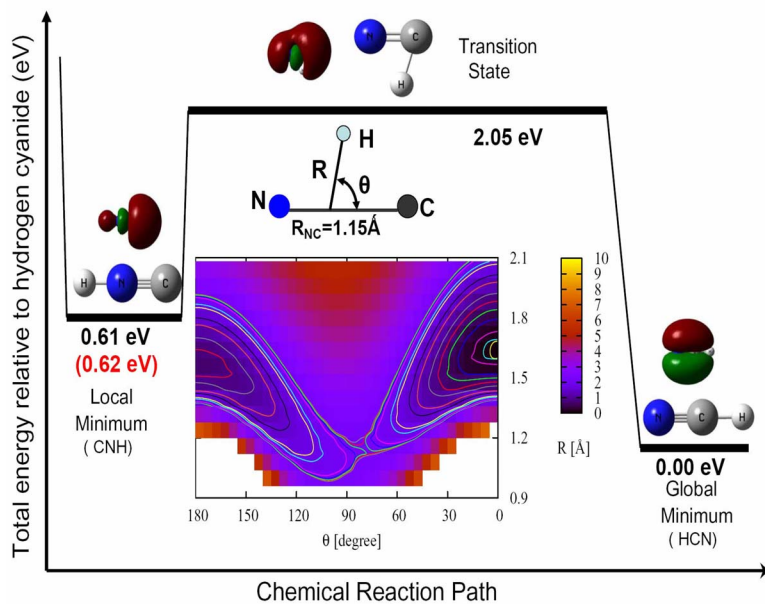


FIG. 15. (Color online) Reaction path of hydrogen cyanide HCN to hydrogen isocyanide CNH calculated by DFT with hybrid B3LYP functional and 6-311+G(2df,2pd) Gaussian-type basis set. The value in parentheses is from experiment [48]. The contour plot of the potential energy surface at the equilibrium distance ($R_{NC} = 1.15 \text{ \AA}$) of the most stable isomer HCN is shown.

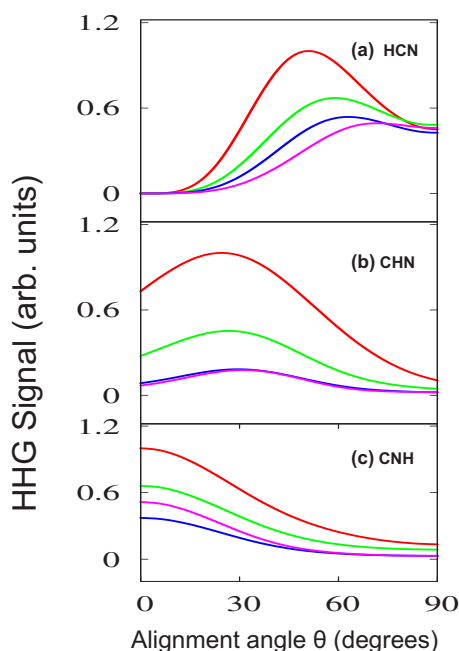


FIG. 16. (Color online) Predicted angular dependence of the 21st, 25th, 29th, and 31st harmonic yields in the plateau region for HCN isomers: (a) hydrogen cyanide HCN, (b) transition state CHN, and (c) hydrogen isocyanide CNH. For (a) and (b) the curves should be read from the top to the bottom. For (c) the curves (from top to bottom) represent the 21st, 25th, 31st, and 29th harmonic.

for the three “molecules” are rather different, and these differences are easily revealed from the large difference in the alignment dependence of the HHG yields shown in Fig. 16, calculated again using the Lewenstein model. Imaging the transition from HCN to HNC via the transition state using HHG would appear to be much simpler in this case. (We comment that in this example, the Coulomb explosion technique probably would be the easiest since there are only three atoms in the system.)

In the discussion so far, the molecules have been assumed to be stationary with their major axis making an angle θ with respect to the laser polarization. Linear molecules can be aligned by a short linear-polarized laser or oriented in a combined dc field and a laser [50]. For more complex molecules, they can be oriented with an elliptically polarized laser pulse [40]. Clearly the orientation and alignment of the molecules itself is a challenging subject on its own. With the rapid progress of laser technology, we are optimistic that HHG from aligned and/or oriented molecules will become available for dynamic imaging in the coming years.

VI. SUMMARY AND FUTURE DIRECTIONS

In this paper we examined the theoretical basis of the tomographic method used by Itatani *et al.* [15]. Due to the limited spectral range provided by the high-order harmonics in the plateau region, we show that intrinsically it is very

difficult to reconstruct accurately the wave function of the highest occupied molecular orbital from the measured high-order harmonics, but the symmetry of the HOMO and the internuclear separation can indeed be adequately obtained. The tomographic method relies on extracting the dipole moment of individual molecules from the HHG measured in a macroscopic medium and that the continuum wave functions in the dipole moment of a molecule be represented by plane waves. The former posts many practical difficulties owing to the macroscopic propagation effect and the imperfect alignment of molecules in the laser field. For the latter, representing continuum wave functions of a molecule by plane waves is a drastic simplification. These limitations pose severe obstacles in any attempt to improve the tomographic imaging of molecules.

In view of the limitations of the tomographic method, we have proposed an iterative approach to extract molecular structure information in the future. The method relies on an efficient and relatively accurate theoretical model for calculating HHG from molecules. With the availability of such a theory, the propagation effect and other macroscopic effects can be modeled to generate HHG that can be compared to the measured data. However, such a simple theory for the HHG by molecules is not yet available today. On the other hand, the alignment dependence of the HHG emission is very sensitive to the nature of the HOMO. If the HOMO changes significantly when the molecule undergoes a transformation—for example, in isomerization—then the HHG yield would reveal the changes efficiently. Using HHG calculated from the Lewenstein model for the isomerization of C_2H_2 and of HCN, we showed that dynamic chemical imaging with HHG is likely possible even without the detailed quantitative iterative procedures outlined in Sec. V.

Still many challenges remain for dynamic chemical imaging with lasers. Theoretically it is imperative that a simple and accurate theory of HHG from molecules be developed. Experimentally, techniques for efficiently aligning molecules with lasers are needed. Since the HHG yield from each molecule is small, the fraction of molecules that undergo chemical transformation should be large within the target volume. Because HHG can also be generated from unexcited ground-state molecules, the intensity of the probe lasers should be selected appropriately. One advantage of using HHG for chemical imaging is that it actually probes the HOMO instead of the atomic positions of the whole molecule; thus, it is much more directly relevant to chemical transformation since it is the change of the outermost electron orbital that dictates chemical reactions.

ACKNOWLEDGMENTS

We acknowledge discussions with David M. Villeneuve and Paul B. Corkum on the details of their tomographic procedure as well as their results [16,32] prior to publication. This work was supported in part by Chemical Sciences, Geosciences and Biosciences Division, Office of Basic Energy Sciences, Office of Science, U.S. Department of Energy.

- [1] A. H. Zewail, *J. Phys. Chem. A* **104**, 5660 (2000).
- [2] H. Ihee, V. A. Lobastov, U. M. Gomez, B. M. Goodson, M. Srinivasan, C. Y. Ruan, and A. H. Zewail, *Science* **291**, 458 (2001).
- [3] A. H. Zewail, *Annu. Rev. Phys. Chem.* **57**, 65 (2006).
- [4] T. Suzuki, *Annu. Rev. Phys. Chem.* **57**, 555 (2006).
- [5] A. S. Alnaser, C. M. Maharjan, X. M. Tong, B. Ulrich, P. Ranitovic, B. Shan, Z. Chang, C. D. Lin, C. L. Cocke, and I. V. Litvinyuk, *Phys. Rev. A* **71**, 031403(R) (2005).
- [6] X. X. Zhou, X. M. Tong, Z. X. Zhao, and C. D. Lin, *Phys. Rev. A* **71**, 061801(R) (2005); **72**, 033412 (2005).
- [7] M. Lein, *Phys. Rev. Lett.* **94**, 053004 (2005).
- [8] S. Baker, J. S. Robinson, C. A. Haworth, H. Teng, R. A. Smith, C. C. Chirila, M. Lein, J. W. G. Tisch, and J. P. Marangos, *Science* **312**, 424 (2006).
- [9] M. Lein, N. Hay, R. Velotta, J. P. Marangos, and P. L. Knight, *Phys. Rev. Lett.* **88**, 183903 (2002).
- [10] T. Kanai, S. Minemoto, and H. Sakai, *Nature (London)* **435**, 470 (2005).
- [11] C. Vozzi, F. Calegari, E. Benedetti, R. Berlasso, G. Sansone, S. Stagira, M. Nisoli, C. Altucci, R. Velotta, R. Torres, E. Heesel, N. Kajumba, and J. P. Marangos, *J. Phys. B* **39**, S457 (2006).
- [12] M. Spanner, O. Smirnova, and M. Yu. Ivanov, *J. Phys. B* **37**, L243 (2004).
- [13] S. N. Yurchenko, S. Patchkovskii, I. V. Litvinyuk, P. B. Corkum, and G. L. Yudin, *Phys. Rev. Lett.* **93**, 223003 (2004).
- [14] S. X. Hu and L. A. Collins, *Phys. Rev. Lett.* **94**, 073004 (2005).
- [15] J. Itatani, J. Levesque, D. Zeidler, H. Niikura, H. Pepen, J. C. Kieffer, P. B. Corkum, and D. M. Villeneuve, *Nature (London)* **432**, 867 (2004).
- [16] S. Patchkovskii, Z. X. Zhao, T. Brabec, and D. M. Villeneuve, *Phys. Rev. Lett.* **97**, 123003 (2006).
- [17] W. H. E. Schwarz, *Angew. Chem., Int. Ed.* **45**, 1508 (2006).
- [18] See <http://online.kitp.ucsb.edu/online/atto06/moletomo/>.
- [19] R. Santra and A. Gordon, *Phys. Rev. Lett.* **96**, 073906 (2006).
- [20] K. C. Kulander, K. J. Schafer, and J. L. Krause, in *Super Intense Laser-Atom Physics*, edited by B. Piraux, Vol. 316 of NATO Advanced Study Institute Ser. B: Physics, Plenum Press, New York, 1993), p. 95.
- [21] P. B. Corkum, *Phys. Rev. Lett.* **71**, 1994 (1993).
- [22] M. Lewenstein, Ph. Balcou, M. Yu. Ivanov, A. L'Huillier, and P. B. Corkum, *Phys. Rev. A* **49**, 2117 (1994).
- [23] P. Antoine, A. L'Huillier, and M. Lewenstein, *Phys. Rev. Lett.* **77**, 1234 (1996).
- [24] P. Balcou, R. Haroutunian, S. Sebban, G. Grillon *et al.*, *Appl. Phys. B: Lasers Opt.* **74**, 509 (2002).
- [25] M. W. Schmidt *et al.*, *J. Comput. Chem.* **14**, 1347 (1993).
- [26] J. Itatani, D. Zeidler, J. Levesque, M. Spanner, D. M. Villeneuve, and P. B. Corkum, *Phys. Rev. Lett.* **94**, 123902 (2005).
- [27] C. Vozzi, F. Calegari, E. Benedetti, J.-P. Caumes, G. Sansone, S. Stagira, M. Nisoli, R. Torres, E. Heesel, N. Kajumba, J. P. Marangos, C. Altucci, and R. Velotta, *Phys. Rev. Lett.* **95**, 153902 (2005).
- [28] A. T. Le, X. M. Tong, and C. D. Lin, *Phys. Rev. A* **73**, 041402(R) (2006).
- [29] T. Brabec and F. Krausz, *Rev. Mod. Phys.* **72**, 545 (2000).
- [30] N. Hay, M. Lein, R. Velotta, R. de Nalda, E. Heesel, M. Castillejo, P. L. Knight, and J. P. Marangos, *J. Mod. Opt.* **50**, 561 (2003).
- [31] G. L. Kamta and A. D. Bandrauk, *Phys. Rev. A* **71**, 053407 (2005).
- [32] J. Levesque, D. Zeidler, J. P. Marangos, P. B. Corkum, and D. M. Villeneuve, *Phys. Rev. Lett.* **98**, 183903 (2007).
- [33] X. M. Tong, Z. X. Zhao, and C. D. Lin, *Phys. Rev. A* **66**, 033402 (2002).
- [34] A. C. Kak and M. Slaney, *Principles of Computerized Tomographic Imaging* (Society for Industrial and Applied Mathematics, New York, 2001).
- [35] D. M. Villeneuve (private communication).
- [36] P. M. Paul, E. S. Toma, P. Breger, G. Mullot, F. Auge, P. Balcou, H. G. Muller, and P. Agostini, *Science* **292**, 1689 (2001).
- [37] Y. Mairesse, A. de Bohan, L. J. Frasinski, H. Merdji, L. C. Dinu, P. Monchicourt, P. Breger, M. Kovacev, R. Taieb, B. Carre, H. G. Muller, P. Agostini, and P. Salieres, *Science* **302**, 1540 (2003).
- [38] H. Wabnitz, Y. Mairesse, L. J. Frasinski, M. Stankiewicz, W. Boutu, P. Breger, P. Johnsson, H. Merdji, P. Monchicourt, P. Salieres, K. Varju, M. Vitteau, and B. Carre, *Eur. Phys. J. D* **40**, 305 (2006).
- [39] M. J. Frisch *et al.*, compute code GAUSSIAN 03, revision C.02, Gaussian, Inc., Pittsburgh, PA, 2003.
- [40] H. Stapelfeldt and T. Seideman, *Rev. Mod. Phys.* **75**, 543 (2003).
- [41] T. Osipov, C. L. Cocke, M. H. Prior, A. Landers, Th. Weber, O. Jagutzki, L. Schmidt, H. Schmidt-Böcking, and R. Dörner, *Phys. Rev. Lett.* **90**, 233002 (2003).
- [42] K. M. Ervin, J. Ho, and W. C. Lineberger, *J. Chem. Phys.* **91**, 5974 (1989).
- [43] S. Boyé-Peronne, D. Gauyacq, and J. Liévin, *J. Chem. Phys.* **124**, 214305 (2006).
- [44] P. Hohenberg and W. Kohn, *Phys. Rev.* **136**, B864 (1964); W. Kohn and L. J. Sham, *Phys. Rev.* **140**, A1133 (1965).
- [45] J. P. Perdew, K. Burke, and M. Ernzerhof, *Phys. Rev. Lett.* **78**, 1396 (1997).
- [46] E. Weigold, S. T. Hood, and P. Teubner, *Phys. Rev. Lett.* **30**, 475 (1973).
- [47] M. Takahashi, N. Watanabe, Y. Khajuria, Y. Udagawa, and J. H. D. Eland, *Phys. Rev. Lett.* **94**, 213202 (2005).
- [48] J. M. Bowman, B. Gazdy, J. A. Bentley, T. J. Lee, and C. E. Dateo, *J. Chem. Phys.* **99**, 308 (1993).
- [49] A. D. Becke, *J. Chem. Phys.* **98**, 5648 (1993).
- [50] H. Sakai, S. Minemoto, H. Nanjo, H. Tanji, and T. Suzuki, *Phys. Rev. Lett.* **90**, 083001 (2003).